Article

Radiative Energy Flux Variation from 2001–2020

Hans-Rolf Dübal [1,*] and Fritz Vahrenholt [2]

[1] Am Langenstück 13, 65343 Eltville, Germany

[2] Department of Chemistry, University of Hamburg, Papenkamp 14, 22607 Hamburg, Germany; fritz.vahrenholt@chemie.uni-hamburg.de

[*] Correspondence: duebal@t-online.de

Abstract: Radiative energy flux data, downloaded from CERES, are evaluated with respect to their variations from 2001 to 2020. We found the declining outgoing shortwave radiation to be the most important contributor for a positive TOA (top of the atmosphere) net flux of 0.8 W/m^2 in this time frame. We compare clear sky with cloudy areas and find that changes in the cloud structure should be the root cause for the shortwave trend. The radiative flux data are compared with ocean heat content data and analyzed in the context of a longer-term climate system enthalpy estimation going back to the year 1750. We also report differences in the trends for the Northern and Southern hemisphere. The radiative data indicate more variability in the North and higher stability in the South. The drop of cloudiness around the millennium by about 1.5% has certainly fostered the positive net radiative flux. The declining TOA SW (out) is the major heating cause (+1.42 W/m^2 from 2001 to 2020). It is almost compensated by the growing chilling TOA LW (out) (−1.1 W/m^2). This leads together with a reduced incoming solar of −0.17 W/m^2 to a small growth of imbalance of 0.15 W/m^2. We further present surface flux data which support the strong influence of the cloud cover on the radiative budget.

Keywords: radiative energy flux; CERES; shortwave flux; longwave flux; cloud thinning

1. Introduction

In the big picture, climate variations originate from variations of the radiative balance at the top of atmosphere (TOA). Surpluses of the EEI (Earth energy imbalance) or net radiative energy fluxes, as measured by satellite mounted radiometers, lead to an increase of the climate system enthalpy and vice versa [1–4]. For about two decades, the CERES Energy Balanced and Filled (EBAF) Ed4.1 [5,6] offers datasets for a variety of radiative fluxes, and, thus, provides a basis to scrutinize the radiative climate driving forces and shine light on the cause-and-effect relation between radiation and temperature change.

As an independent but less direct source of information of the climate system enthalpy change, there are several studies and reconstructions [7–12] of the ocean heat content (OHC) which represents the bulk of the climate system enthalpy, estimated to be about 90%. Assuming this fraction of 90% were a longer-term constant, one can trace back the time-development of the climate system enthalpy. Von Schuckmann et al. [13] have combined radiative, ocean heat and other data to reconstruct an enthalpy curve back to 1960 and have found an accelerated heating since 2010. Recently, Loeb et al. [14] found a good agreement between radiative (CERES) and OHC data for the period mid-2005 to mid-2019. These authors have further studied the influencing factors for the shortwave (SW) and longwave (LW) radiative fluxes and concluded that cloud changes have fostered the downwelling shortwave radiation.

Dewitte et al. [15] have analyzed CERES datasets for the period from 2000 to 2018 and found an EEI value of about 0.9 W/m^2 but with a declining trend going in line with a declining time-derivative of the latest OHC data obtained from Cheng et al. [9]. Based upon recent CERES data, Loeb et al. [16], Wong et al. [17] and Ollila [18] reported an increasing

downwelling shortwave (SW) radiation. Loeb et al. reported a decreasing TOA SW trend, mainly caused by a reduction in low cloud cover, and Ollila concluded that this increasing downwelling SW, which is particularly strong since 2014, may be responsible for a new wave of heating after the hiatus. This finding is in conflict with the assumption that further global warming originates mainly from the LW radiation capture caused by greenhouse gases, i.e., a decline of outgoing LW.

The obvious and substantial, if not overwhelming role of clouds for the radiation budget and climate system enthalpy and, hence, for the question about the root cause of the further development of global warming, is nowadays still a vaguely known factor. The cloud-albedo feedback is deemed to be essential for climate modeling [19] but is still poorly understood. According to a cloudiness dataset from EUMETSAT/CM SAF [20] there was a significant drop in global cloudiness around the year 2000, which has not yet fully recovered, and which certainly has affected the radiative net flux in the time-period considered here. In this paper, we report radiative flux data and trends in cloudy and cloud-free regions, obtained from CERES and other sources and relate them to the TOA and surface radiative budgets and climate system enthalpy. We further attribute the differences between the Northern and the Southern hemisphere.

Finally, we discuss these results in a longer-term context and suggest a possible correlation of cloud cover shifts such as the one around the millennium with the AMO (Atlantic Multidecadal Oscillation).

2. Datasets and Evaluation

We have downloaded the datasets presented and analyzed here as monthly averages from Jan-2001 to Dec-2020, obtained from the NASA Langley Research Centre CERES [5,6] ordering tool at (http://ceres.larc.nasa.gov/), (accessed on 29 July 2021), spatial resolution $1° \times 1°$, unless marked otherwise. The changes from Edition 4.0 [5,6] to Edition 4.1 are summarized in: https://ceres.larc.nasa.gov/documents/DQ_summaries/CERES_EBAF_Ed4.1_DQS.pdf (accessed on 29 July 2021). We transformed them into annual averages and used these annual averages without further changes. Only the datasets marked as "Cloudy Areas" were calculated by the authors from the "All Sky" and the "Clear Sky (for cloud-free areas of region)" data according to Equation (1), year by year, making use of the annual averages of CERES "cloud area fraction" (abbreviated as c) and with obvious notation for the fluxes (F) involved.

$$F_{Cloudy\_Areas} = [F_{All\_Sky} - (1 - c) \times F_{Clear\_Sky}]/c \qquad (1)$$

To interpret the results, it is of some importance to realize the wavelength channels in CERES, which are:

Channel	Wavelength/μm
TOT (Total flux)	0.3–200
SW (Shortwave flux)	0.3–5
LW (Longwave flux)	5–200

Hence, the infrared active molecular vibrations and rotations of the greenhouse gases fall into different categories: fundamental bending and deformation vibrations (H_2O, CO_2, CH_4, etc.) as well as rotations (H_2O) are in the LW-range and the OH (oxygen-hydrogen bond) and CH (carbon-hydrogen bond) stretching vibrations of H_2O and CH_4 including their overtone and combination band spectra fall into SW. Even the asymmetric stretching vibration of carbon dioxide falls into the SW. That means that not only the LW but also the SW fluxes are influenced by infrared absorption.

The effective TOA ("Top of Atmosphere") focal height of CERES is ca. 20 km. Surface fluxes as well as "Cloud Effective Temperature" and "Cloud Area Fraction" are provided by CERES, transformed into annual averages without further changes with the exception of the "Cloudy Areas" as explained above.

Two other datasets ("cloudiness" and "OLR" (outgoing longwave radiation)) were downloaded from the WMO (World Meteorological Organisation) homepage (http://climexp.knmi.nl/get_index.cgi, accessed on 29 July 2021) as monthly averages [20], transformed to annual averages ("HIRS" stands for "High-Resolution Infrared Radiation Sounder").

OHC ("Ocean Heat Content") data were graphically extracted from the quoted literature [7–12].

Enthalpy data were calculated from the TOA radiative fluxes by means of Equation (2).

$$\Delta H = A \times (\text{Inc\_Solar} - \text{LW}_{OUT} - \text{SW}_{OUT}) \times 365.25 \times 24 \times 60 \times 60/1 \text{ E21} \qquad (2)$$

with:

A = 5.10 E14 m^2 (Earth surface);

Inc_Solar = TOA incoming solar radiative flux (W/m^2), annual mean value;

LW_{OUT} = TOA outgoing longwave radiative flux (W/m^2), annual mean value;

SW_{OUT} = TOA outgoing shortwave radiative flux (W/m^2), annual mean value
365.25×24×60×60 = 31,557,600 s per year.

The division by 1E21 yields the unit ZJ (Z = 1 E21) for the enthalpy.

Statistical error analysis is made by means of linear regression and summarized in the Appendix A. It includes the slope (trend) and errors, *p*-value, R^2 and confidence intervals. In the main text, we are just referring to a statistical uncertainty in the form x ± Δx. Details can be seen in the Appendix A.

In the text, we use the absolute values of the fluxes (in W/m^2), respectively, their actual changes from 2001 to 2020 as well as the statistical trend data (in W/m^2 per decade). The further are used to discuss the actual changes, whereas the latter are linear estimations and specify the average tendencies.

3. Results and Discussion: Top of Atmosphere (TOA) Radiative Balance

Figures 1–4 show the incoming solar, the outgoing shortwave (SW), the outgoing longwave (LW) and the net radiative fluxes for "All Sky" conditions, which includes "Cloudy Areas" and "Clear Sky" areas. The figures include the global, Northern (NH) and Southern (SH) hemispheric fluxes. The incoming solar irradiation is slightly decreasing in the total window of 0.3 to 200 μm, whereas as the outgoing LW flux became stronger during the last two decades. These both effects alone would have diminished the climate system's enthalpy, if not the reduction of the outgoing shortwave flux would have overcompensated these two effects. This SW effect caused an increasing net flux during these two decades. Loeb et al. [16] and Ollila [18] had already noticed the declining SW (out) which corresponds to an increasing downwelling SW trend, because the incoming solar flux was almost constant during the period of time considered.

Dewitte et al. [15] have analyzed CERES data until 2017, and found a positive TOA net flux but with a declining trend. In the data presented here, the TOA net flux has a similar average positive value but is slightly rising with time. The TOA net flux is a tiny difference of large numbers and is therefore prone to a rather large relative uncertainty. Therefore, the authors are unable to decide whether the trend is, actually, going up or down.

The TOA net flux was +0.75 W/m^2 in 2020. The data shown in Figures 1–3 suggest that the root cause for the positive TOA net flux and, hence, for a further accumulation of energy during the last two decades was a declining outgoing shortwave flux and not a retained LW flux. The dominating influence of a declining TOA outgoing SW is not in line with the assumption that the global warming in the last 20 years is primarily caused by holding back the LW due to the greenhouse effect. As discussed below, the greenhouse effect plays a role, however, for the period 2001–2020 at TOA it was certainly not dominating.
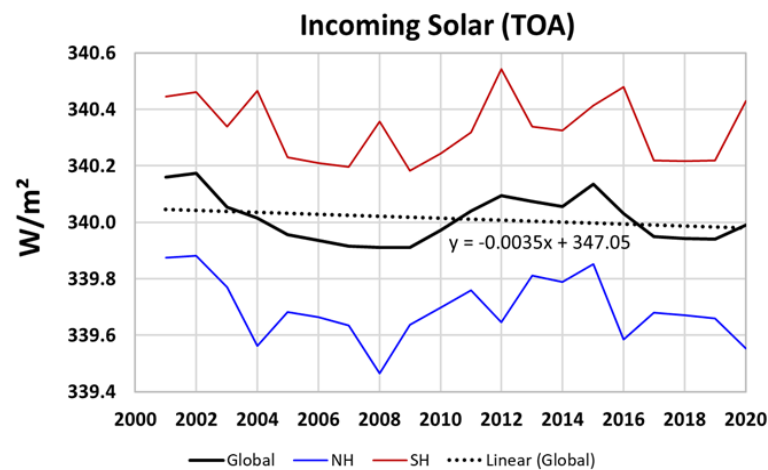
Figure 1. The weakly declining annual mean value (-0.07 ± 0.06 W/m^2) of the incoming solar irradiation for the globe, NH and SH. The Southern hemisphere obtains ca. 0.7 W/m^2 more than the North due to the eccentric orbit and the inclined axis of the Earth.
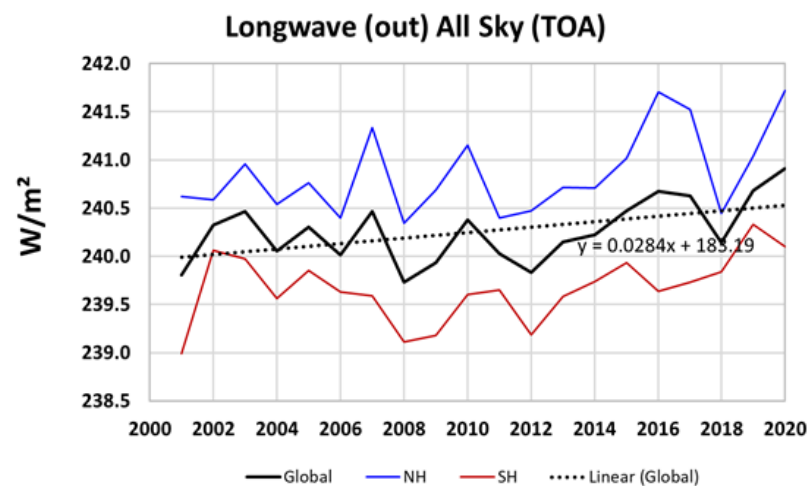

Figure 2. The increasing trend of the LW flux. The average effect is $+0.6 \pm 0.2$ W/m^2 for two decades. The Northern hemisphere is warmer than the South and therefore shows a higher LW (out) value.
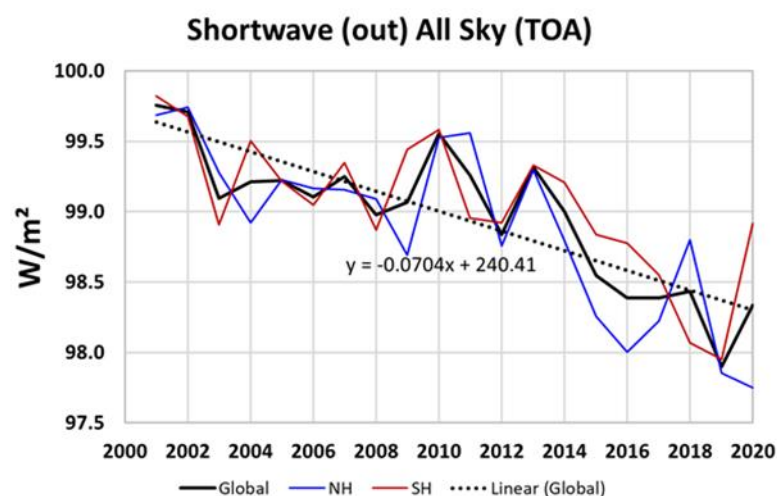

Figure 3. The declining trend of the outgoing SW flux at TOA. The average effect is -1.4 ± 0.2 W/m^2 for two decades, stronger than both effects shown in Figures 1 and 2 combined. Other than above, there are no significant differences between NH and SH.
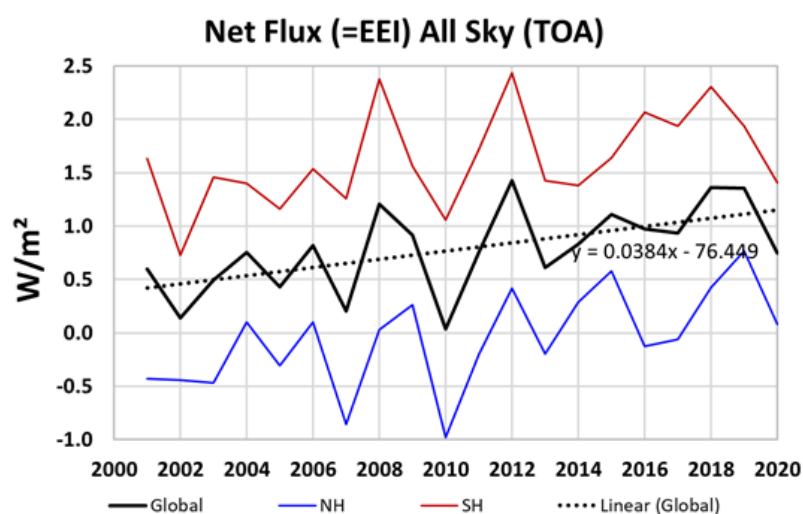
Figure 4. TOA net flux for global, NH, and SH. The Southern hemisphere obtains a higher flux (+ 1.7 W/m²) than the North which is due to the aphelion/perihelion of the Earth's rotation around the sun, resulting in a stronger radiative flux during the SH summer, not compensated by the weaker SH winter. Nevertheless, the NH has warmed up more strongly during the given period of time.

Some residual uncertainty remains regarding the sign of the TOA net flux. By simply adding the uncertainties of the gross in- and outgoing fluxes, the uncertainty of the difference could easily be in the order of 1 W/m² or more, which is larger than the 0.75 W/m² reported for the year 2020. However, as shown below, the independently observed OHC data comply well with a positive radiative net flux, and it can be rather safely assumed that there was indeed a positive net flux during the last two decades.

The declining outgoing SW was mainly caused by less reflected solar light which points towards the role of the clouds. Only a minor SW portion may be absorbed by the increasing amount of water vapor by means of their OH stretching vibrations (ca. 3 µm) and overtone, respectively combination band absorption (ca. 1.9 µm, 1.5 µm, 1.0 µm, etc.). Figure 5 compares outgoing SW under "Clear Sky" conditions (left side) with the "Cloudy Areas" (right side) using identical scale ranges. The decline is pronounced in the NH and the absolute effect is greater over the "Cloudy Areas". The "Clear Sky" SH trend is almost flat. Over the clouds, we find a declining trend in NH and SH, still stronger in the North but with a visible decline in the South also. It seems as if the trend accelerated around 2010–2014. In fact, for the global "Cloudy Areas" data the slope is −0.043 W/m²a for 2001–2010 and −0.16 W/m²a for 2011–2020, i.e., four times larger.
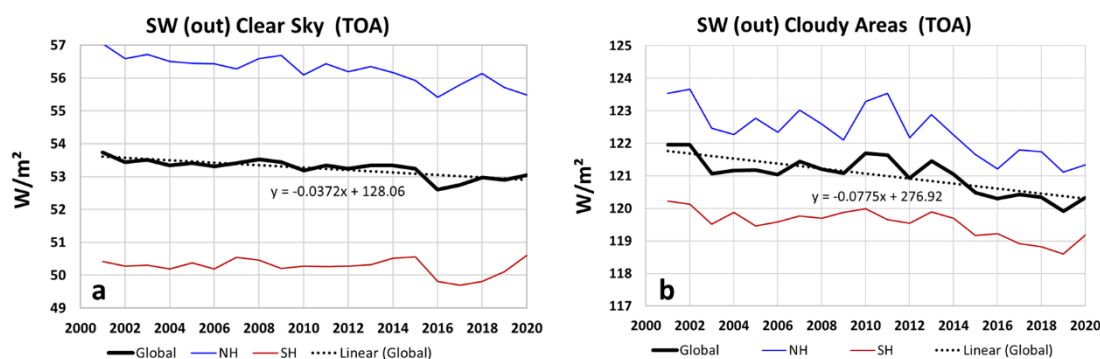
Figure 5. Shortwave outgoing radiative flux (TOA) over "Clear Sky" (**a**) and "Cloudy Areas" (**b**) for global average, NH, and SH. Please note, there is an apparent inconsistency when comparing these plots with Figure 3, in which there is no significant difference between NH and SH. The reason is a different average cloud area fraction of about 70% in the South and 64% in the North. Therefore, the cloud-area-weighted "All Sky" data are very similar.

The changes in the cloud albedo are overwhelming the changes of the land/ocean albedo. If we define surface albedo as the ratio of the TOA outgoing SW and the incoming solar fluxes, we find a reduction from 15.80% to 15.56% (−0.23% absolute) in the "Clear Sky" from 2001 to 2020 stemming from changes in the land and ocean surface. In the "Cloudy Areas" we find a much stronger reduction from 35.85% to 35.28% (−0.58% absolute). The "All Sky" values changed from 29.33% to 28.80% (−0.53% absolute). The area-weighted effect of the albedo change is −0.08% (absolute) for the land/ocean part and −0.39% (absolute) for the clouds. The cloud effect on the albedo change is 5.2 times larger than the land/ocean effect. In other terms, about 15% of the observed albedo change is due to the diminishing land/ocean albedo, and 85% is due to the diminishing cloud albedo. Hartmann and Ceppi [21] as well as Dewitte et al. [15] have studied the influence of sea ice extend (SIE) in the Northern polar region on the reflected SW and found a good correlation of the "Clear Sky" reflected solar light with SIE for that region. We also find such a pronounced regional effect, however, it is limited to a too small area to explain the globally declining "All Sky" outgoing SW presented here.

The outgoing TOA LW flux shows a different trend. Figure 6 reveals the increasing LW flux which is much steeper over the clouds (0.35 ± 0.13 W/m^2 per decade) than over the clear sky (0.04 ± 0.1 W/m^2 per decade) which is essentially constant. Furthermore, there is a striking difference between North and South. The difference between NH and SH is smaller for the "Clear Sky" areas, and the North emits a higher LW flux than the South. For the "Cloudy Areas" the difference between NH and SH is twice as large but the South emits a higher LW flux than the North. The latter goes in line with a higher cloud effective temperature (Figure 7) in the South and the former corresponds to a higher surface temperature on the Northern hemisphere. The smaller absolute value of the flux over the "Cloudy Areas" is due to a lower cloud temperature compared with the surface. Only the much steeper trend for the "Cloudy Areas" is puzzling and points towards a change in the cloud structure.
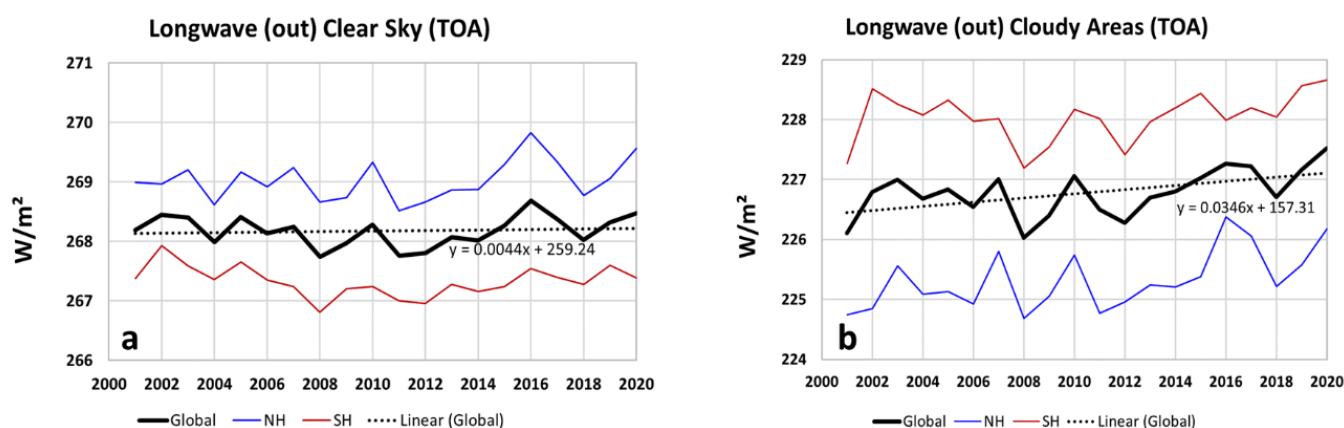
Figure 6. Outgoing longwave flux (TOA) over "Clear Sky" (**a**) and "Cloudy Areas" (**b**). The slope over the "Cloudy Areas" is eight times higher.

The TOA net fluxes over the "Clear Sky" and "Cloudy Areas" exhibit—as expected— a striking difference (Figure 8). The former has a strongly positive ("heating") net flux whereas the latter has a large negative ("cooling") value. About 2/3rds of the sky is covered with clouds of all types, heights, thicknesses and other properties, and the mix of ca. 2/3rd negative flux (Figure 8b) and ca. 1/3rd positive flux (Figure 8a) results in an average net flux shown in Figure 4 above.

Cloud Effective Temperature

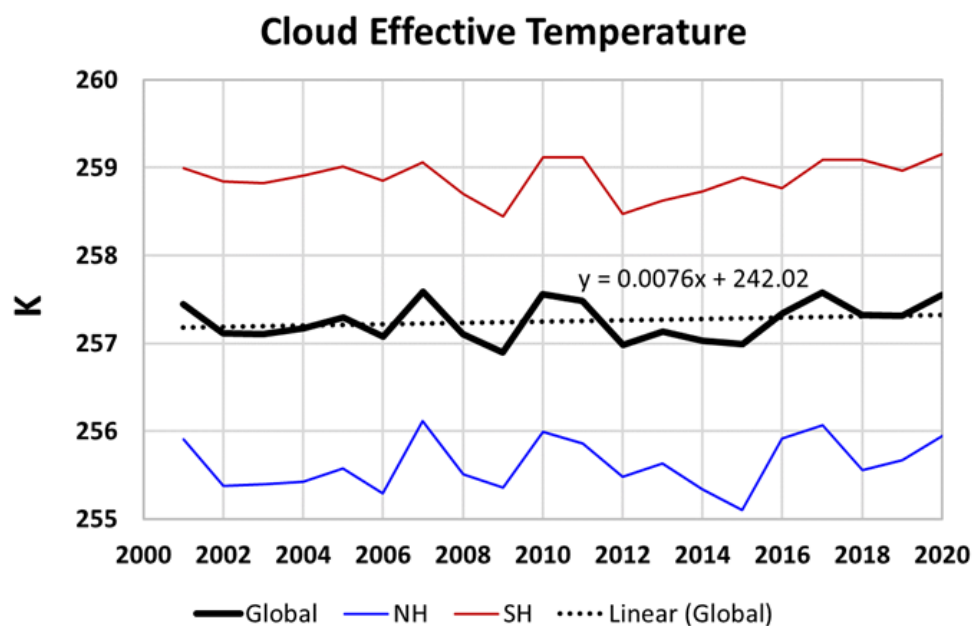**Figure 7.** The effective temperature of the clouds is ca. 3.5 K higher in the Southern hemisphere compared with the North. In 20 years, it has increased by ca. 0.1 K in the SH, by ca. 0.2 K in the NH, and by 0.15 K in the global average. The data were downloaded from CERES. Source: https://ceres.larc.nasa.gov/data/ (accessed on 29 July 2021).
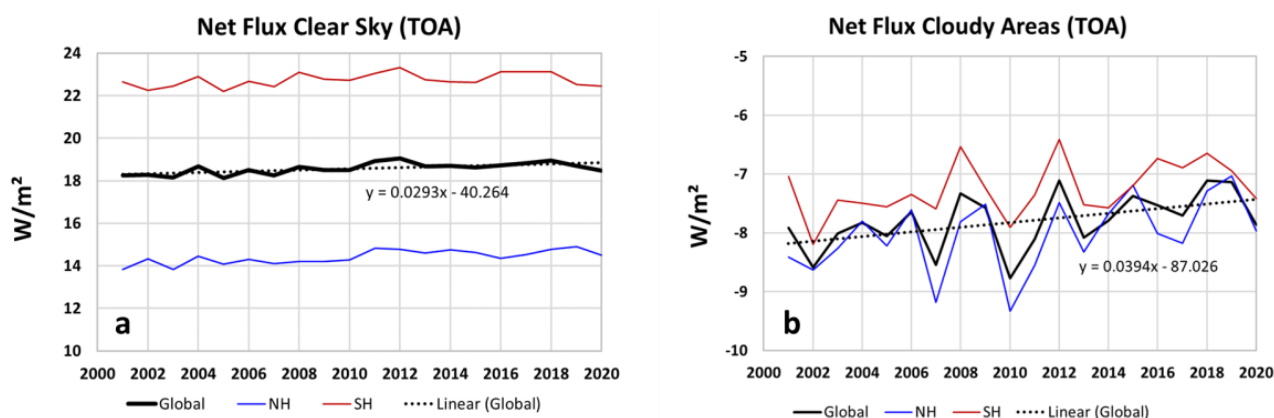

Figure 8. Net flux (TOA) over "Clear Sky" (**a**) and "Cloudy Areas" (**b**) for global average, NH, and SH. For the global values, the difference between "Clear Sky" and "Cloudy Areas" is 26 W/m². This 1% change of the cloud cover corresponds to 0.26 W/m² flux change.

The difference between NH and SH is much more pronounced over the "Clear Sky", but the rising trend is somewhat steeper over the "Cloudy Areas". The enormous influence of the clouds for the energy balance and, hence, for the climate system enthalpy is obvious. This is also visible from Figure 9 in which the cloudiness and the outgoing LW (here: OLR) are presented for a longer time span. The (inverse) correlation coefficient between OLR and cloudiness is 74%. The cloud window that opened around the year 2000 has certainly fostered the heating. The CERES data agree quite well with the HIRS OLR data, but the comparison also shows that some methodical uncertainties in the order of 1 W/m² must be taken into account.
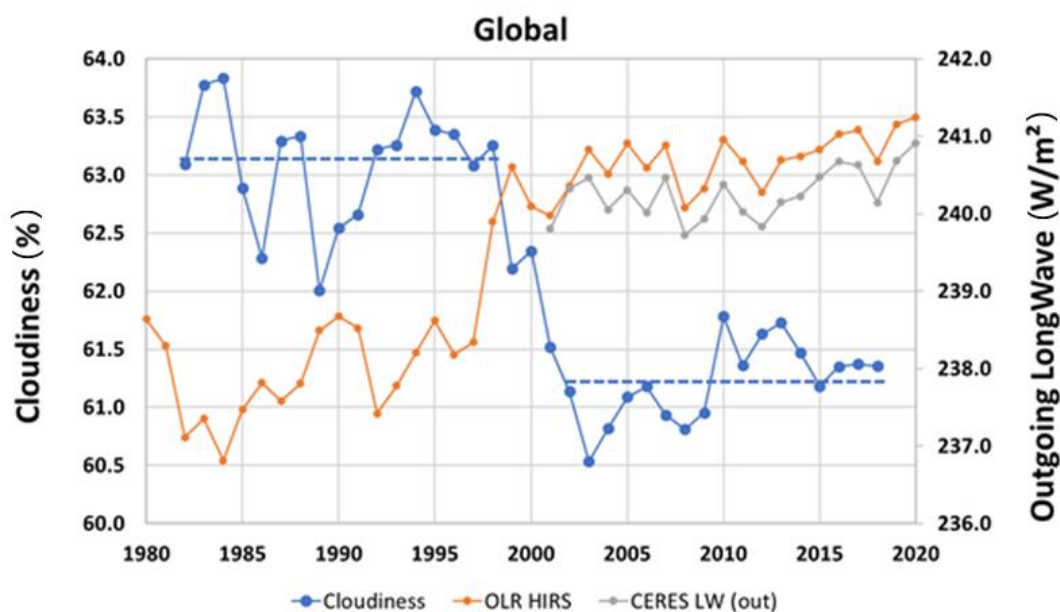
Figure 9. A longer-term plot of the outgoing longwave flux and cloudiness, based upon datasets downloaded from the WMO homepage [20], source: https://climatedata-catalogue.wmo.int/explore accessed on 29 July 2021. The broken lines denote the average of the years before (1982–1997) and after (2003–2018) the drop of the cloud cover. The difference is $-1.86 \pm 0.80\%$.

The terms "cloudiness" and the CERES term "cloud area fraction" have different definition and methodology but both are associated with the cloud cover. The cloudiness is currently ca. 61.3% whereas the cloud area fraction from CERES is ca. 67.5%. Nevertheless, from Figure 8 it follows, that a change of cloud cover by 1% would cause a change of the TOA global net flux of 0.26 W/m^2 so that the drop of 1.86% of cloudiness in Figure 9 could have caused an effect of ca. 0.5 W/m^2, a large portion of the observed average value for 2001–2020 (0.8 W/m^2). Actually, adding the 0.5 W/m^2 to the 20th century average (ca. 0.3 W/m^2) gives the current value.

4. Results and Discussion: Surface Fluxes

CERES data provide an opportunity to differentiate between "Clear Sky" and "Cloudy Areas" not only at TOA, but also for the surface fluxes and this enables us to analyze the influence of clouds on the surface radiation budget as well. At first, under idealized balanced conditions, the TOA radiative budget is exactly zero. At the surface, however, the radiation budget under idealized balanced conditions is far away from zero. It is ca. 110 W/m^2 and this radiative imbalance is compensated by enthalpy changes, mainly by the evaporation of water so that the sum of the overall balance of radiative flux and the time derivative of the enthalpy at the surface strives towards zero.

The surface fluxes show striking differences between "Clear Sky" and "Cloudy Areas" as well. Figure 10 shows SW up- and downwelling surface fluxes for different cloud coverages. While in the "Clear Sky" regions the downwelling SW (Figure 10a) essentially follows the declining incoming solar flux, there is a significantly rising downwelling surface flux (Figure 10c) for the "Cloudy Areas". The upwelling SW fluxes (Figure 10d–f) have similarly declining trends irrespective of the clouds and their absolute values are about 12.5% of the downwelling fluxes (Figure 10a–c), with decreasing trend. The surface SW net flux is rising more pronounced in the "Cloudy Areas" by $+0.93 \pm 0.18$ W/m^2 per decade compared with the "Clear Sky" regions with only $+0.24 \pm 0.10$ W/m^2 per decade. We conclude that the clouds have increased their transmittance for the SW radiation. This is possible by means of changes of the cloud type, height, particle size, phase mix, geographical location, interaction, etc. The parameter "Cloud Optical Density", which is

available from CERES, however, could neither support nor deny this interpretation because the rather high variance prevents to identify a clear trend.
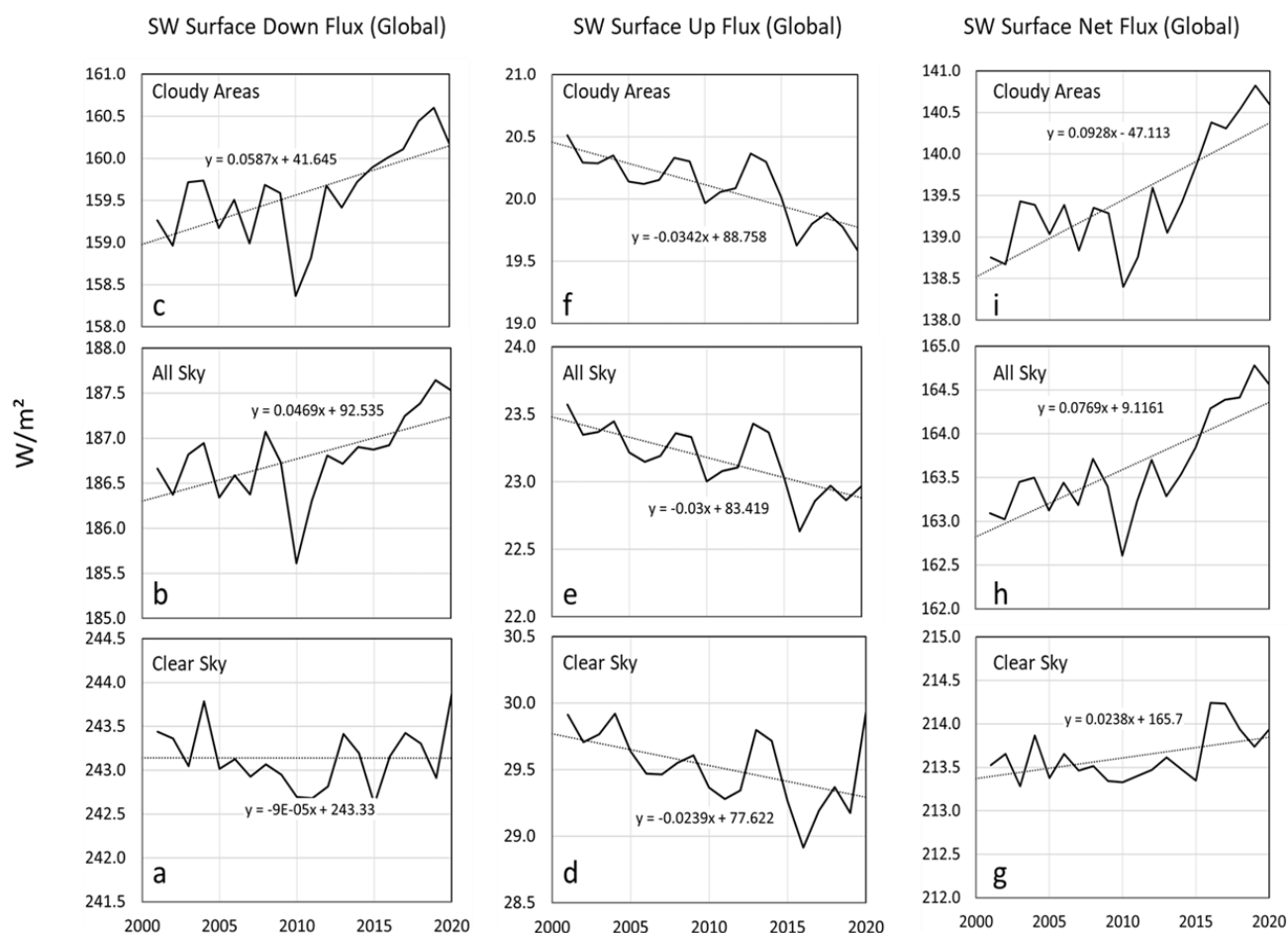

Figure 10. Global average SW downwelling (**a**–**c**), upwelling (**d**–**f**), and net (**g**–**i**) surface fluxes for "Clear Sky", "All Sky", and "Cloudy Areas".

The surface downwelling LW flux (Figure 11) has a different trend than the SW. The "Clear Sky" areas (Figure 11a) show a strongly rising trend, compared with a flat or slightly declining trend in the "Cloudy Areas". In the "All Sky" average, the downwelling LW has a rising trend half as strong as the downwelling SW and with high variance, namely $+0.27 \pm 0.34$ W/m^2 per decade. The LW upwelling fluxes (Figure 11d–f) show strong trends around 1 W/m^2 per decade and are almost independent of the cloud coverage in size and trend. Here, the surface temperature is the main driver, and the radiative flux increases as a function of the surface temperature. The LW net surface fluxes show a strongly declining trend that is accelerating after 2016 with the exception of the "Clear Sky" regions. As a consequence of the rising SW and the falling LW net fluxes, the "All Sky" surface net flux has no clear trend but a significant fluctuation (Figure 12).

At this point, we describe the direct observation of the greenhouse effect, namely by comparing the "Clear Sky" LW upwelling radiation (Figure 11d) and the outgoing TOA LW flux (Figure 6a, left side). The first is rising with $+1.22 \pm 0.22$ W/m^2 per decade, the latter trend is literally flat with $+0.04 \pm 0.10$ W/m^2 per decade. Hence, in the absence of clouds, a large portion of this additional upwelling LW radiation is absorbed by the increasing greenhouse gas concentration (CO_2 has increased from 371 to 414 ppm obtained from https://gml.noaa.gov/webdata/ccgg/trends/co2/co2_annmean_mlo.txt (accessed on 29 July 2021), water from 10.44 to 10.71 g/kg at 1000 mbar from 2001 to 2020 obtained from https://psl.noaa.gov/cgi-bin/data/timeseries/timeseries1.pl, (accessed on 29 July 2021). We

have applied the Lambert–Beer's law and correlated the logarithmic ratio of the outgoing TOA LW flux and the "Clear Sky" LW upwelling flux with the rising greenhouse gas concentrations and found a very good linear correlations for CO_2 ($R^2 = 0.92$) and water vapor ($R^2 = 0.72$).
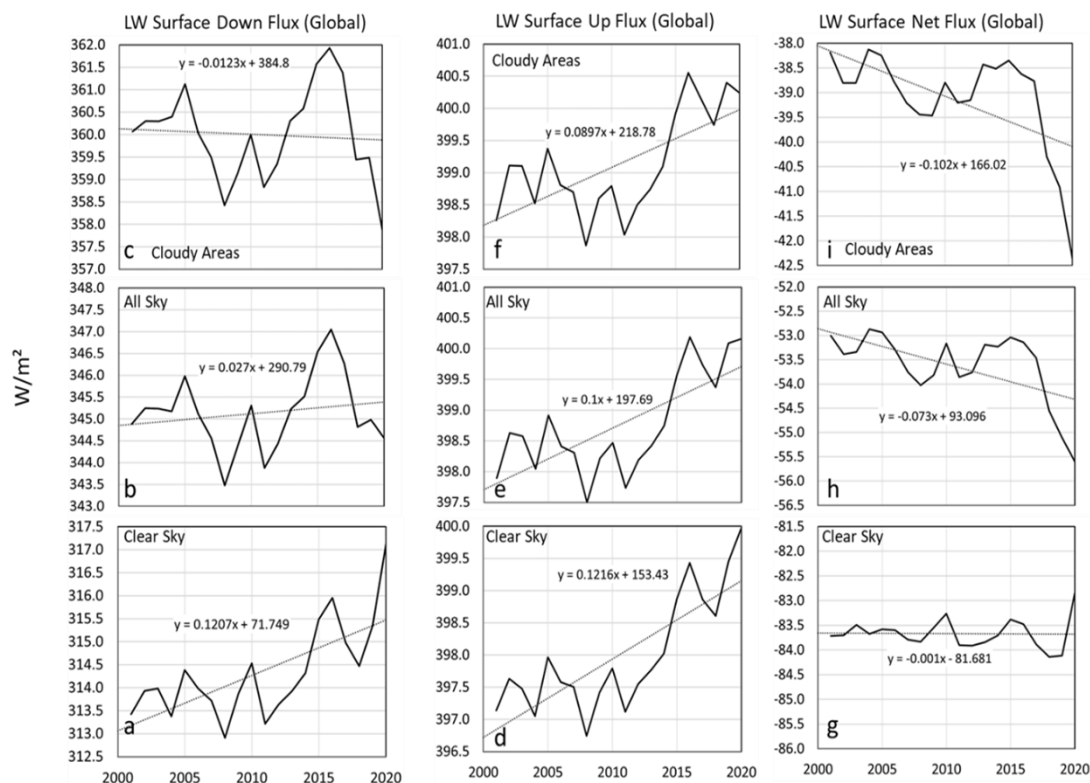
Figure 11. Global average LW downwelling (**a**–**c**), upwelling (**d**–**f**), and net (**g**–**i**) surface fluxes for "Clear Sky", "All Sky", and "Cloudy Areas".
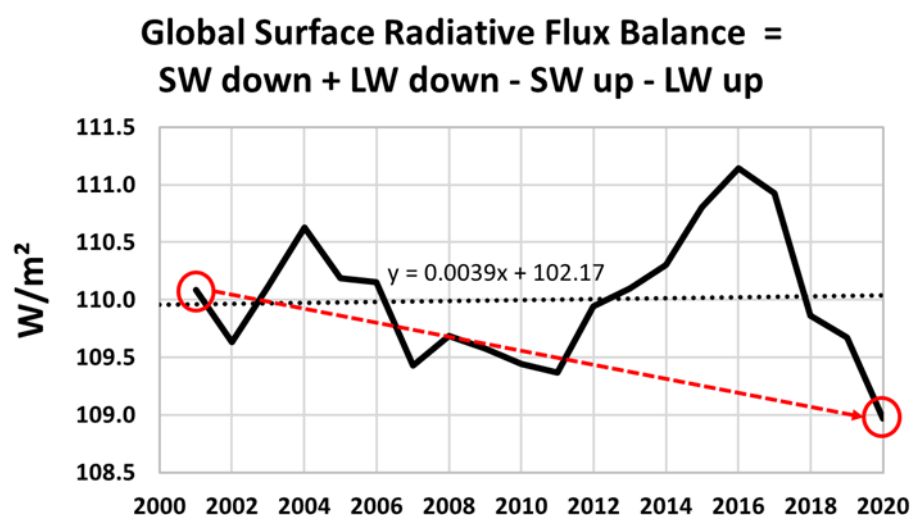
Figure 12. The global "All Sky" surface net flux shows no clear tendency. The 2020 value is below the 2001 value (arrow), and the mean trend is slightly positive but with overwhelming variance.

Another observation is that these correlations vanish for the "Cloudy Areas". The clouds absorb most of the LW flux and are emitting a weaker thermal flux in all directions. The part designated to reach the TOA point has little chance to be absorbed by greenhouse gases because the pathway is shorter, the pressure is lower, the water vapor is sparse, and

the initial flux is weaker. All this works towards much lower infrared absorption above the clouds and the TOA outgoing LW rises with 0.35 ± 0.13 W/m^2 per decade.

In absolute terms, the LW surface upwelling flux is about 398 W/m^2 for "clear sky" (Figure 11d) and only ca. 268 W/m^2 at TOA (Figure 6a) which is an attenuation of 130 W/m^2 or 33%, caused by greenhouse gases, by scattering, and by small clouds below the measurement threshold. In the "Cloudy Areas" we start with about 399 W/m^2 LW surface emission (Figure 11f), which is absorbed by the clouds and re-emitted at a lower temperature of about 258 K (Figure 7). This cloud average temperature corresponds to about 260 W/m^2 emission (estimated from Stefan–Boltzmann's law), and ca. 227 W/m^2 of it reaches the TOA (Figure 6b). The attenuation here is only 33 W/m^2 or 12.6%. There again, the corresponding downwelling back-radiation is absorbed by the clouds and contributes to elevating their temperature. Only a minor share of this smaller part reaches the Earth's surface.

Hence, the rise of the greenhouse gas concentration from 2001 to 2020 had a measurable effect on the LW flux in the "Clear Sky", covering about 1/3rd of the Earth surface. In the cloudy part, about 2/3rd, this effect was much smaller, if significant at all.

5. Effect on the Climate System's Enthalpy

With the one and only exception of radiation, the Earth is an almost perfect adiabatic thermodynamical system. Material exchange, convection and heat diffusion is prevented by gravity and all other sources or mechanism of energy exchange with the environment, the space, such as starlight and cosmic particle flux are negligible in terms of enthalpy. The cosmic particle flux could, however, have a significant indirect effect by its influence on the cloud formation which again provides a very strong leverage for the radiation budget. This potentially very important indirect effect was described by Svensmark [22] and by Shaviv [23].

Radiative datasets are available for only a few decades, however, ocean heat content (OHC) data were reconstructed for much longer and, assuming that constantly ca. 90% of the climate system's enthalpy ended up as ocean heat, provide an opportunity to reconstruct the enthalpy development for a longer period of time. OHC reconstructions were reported by Levitus et al. [7], Roemmich et al. [24], Cheng et al. [10] and Gebbie and Huybers [11]. Von Schuckmann et al. [13] have developed an enthalpy summary for 1971–2018. They also reported the distribution over the various degrees of freedom such as the heat of oceans, air and land, evaporation of water and melting of ice and volume work. Changes of the kinetic energy of air and ocean water would have to be added. They also used CERES radiative data and reported a net flux of 0.87 W/m^2 for 2010–2018, which is larger compared with the longer term mean value of only 0.47 W/m^2 for 1971–2018 and the long-term 0.2 W/m^2 reported by Baggenstos et al. [25]. Earlier, Allen et al. [26] reported net radiative fluxes of 0.34 ± 0.67 W m^2 for the period 1985–1999, and 0.62 ± 0.43 W m^2 for 2000–2012. Roemmich et al. [24] reported a value between 0.4 and 0.6 W/m^2 for the period of 2006–2013 for the 0–2000 m OHC. Recently, Loeb et al. [14] reported a trend of 0.43 ± 0.40 W/m^2 per decade from mid-2005 to mid-2019 for the 0–2000 m OHC, compared with the trend for the net CERES TOA energy flux of 0.50 ± 0.47 W/m^2 per decade over that same time-period. The data analyzed in this paper resulted in a net flux of 0.8 W/m^2 for the period 2001–2020 and this corresponds to an enthalpy increase of about 240 ZJ during this period. However, the root cause of this enthalpy gain is in dispute. This becomes clear from the strong effects of the shortwave radiation changes, the cloud cover changes and, also, from a longer-term development of the enthalpy.

Figure 13 presents a longer-term enthalpy curve, constructed from various sources, radiative and oceanic, the latter under the assumption of a constant 90% OHC share. Figure 14 shows a shorter-term view of the same data. In both figures, the distinct zero-level of each of the enthalpy data was shifted to fit. The current enthalpy is still ca. 600 ZJ below the medieval maximum 1000 years ago grounded on the 2000 years OHC reconstruction reported by Gebbie and Huybers [11]. This would be compensated in only

50 years with the presently observed +0.8 W/m² net flux and in about 100–200 years for the average rate as during the 20th century. With a possible interception by another phase of a negative radiative net flow, it would take centuries until we reach the medieval OHC maximum again.
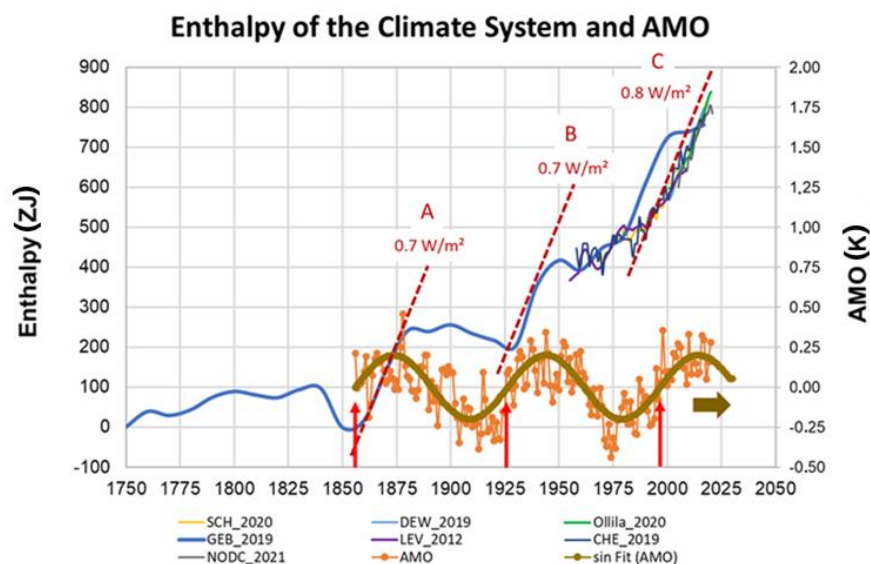

Figure 13. Climate system enthalpy since 1750, reconstructed from radiative and ocean heat data taken from the publications of Schuckmann et al. [13], Ollila [18], Dewitte et al. [15], Levitus et al. [7] and NODC [7], Cheng et al. [10], Gebbie and Huybers [11] and this work. The OHC-Data were divided by 0.9. The two heating impulses A and B had a span of about 25 years, and similarly, high net fluxes as the presently observed phase C. The zero levels of the enthalpy datasets was set to match. The AMO values were downloaded from http://www.psl.noaa.gov/data/timeseries/AMO/ (accessed on 29 July 2021) and transformed into annual averages. A sine-fit is added to the AMO-data (right scale). The arrows at ca. 1860, 1925 and 2000 indicate the sign change of the AMO-Index from negative to positive.
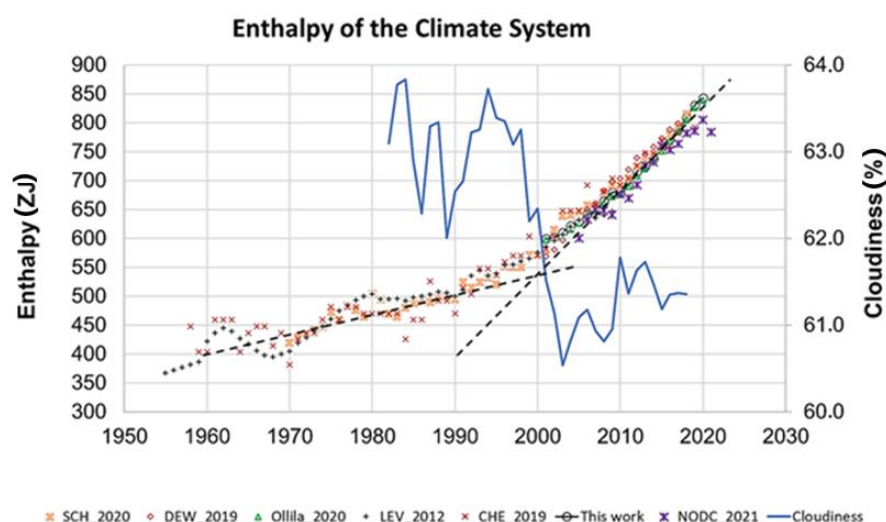
Figure 14. Expanded enthalpy plot. The cloudiness [20] is included (right scale). The rise of the enthalpy after the millennium coincides with the drop of cloudiness. The latest OHC data from NODC exhibit such a flatter tendency for about one year.

Hence, the decisive question is; whether the currently observed strong heating phase C is temporary like the phases A and B in Figure 13 or the beginning of a steadily rising warming period. A third possibility is that phase C is a combination of the natural induced

A/B type and steadily warming. The enthalpy-enhancing effect of the greenhouse gases (including water vapor) is clearly visible in our analysis, however, we found, in line with other authors [14,15,18], that this effect is only one out of several other important factors. In the period 2001–2020, the greenhouse gas effect is prominent in the "Clear Sky" areas but overcompensated by the SW fluxes and cloud effects. This is also evident from the bridge chart in Figure 15 below. As an alternative, the phases A, B and C since 2001 could be interpreted as a kind of "global brightening" phases followed by "global dimming" (for a review of global brightening/dimming see [27]).
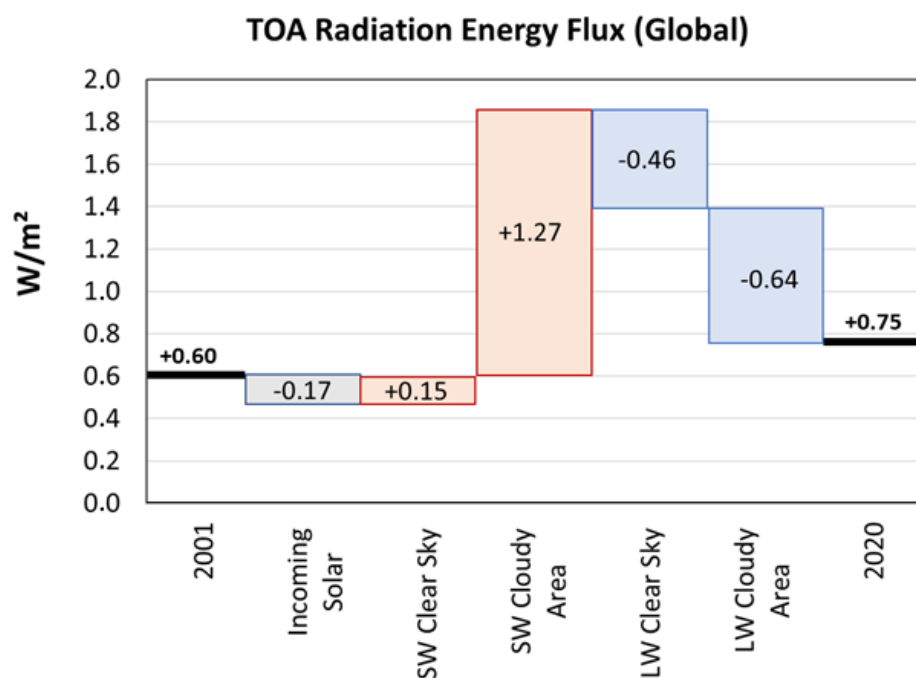

Figure 15. Bridge-chart for the actual changes at TOA from 2001 to 2020 ("start-to-end change"), dominated by the change in the outgoing shortwave radiation over "Cloudy Areas". The declining SW (out) is the major heating cause. It is almost compensated by the chilling LW (out). The incremental effects are weighted by area (see the example in the caption of Figure 16).
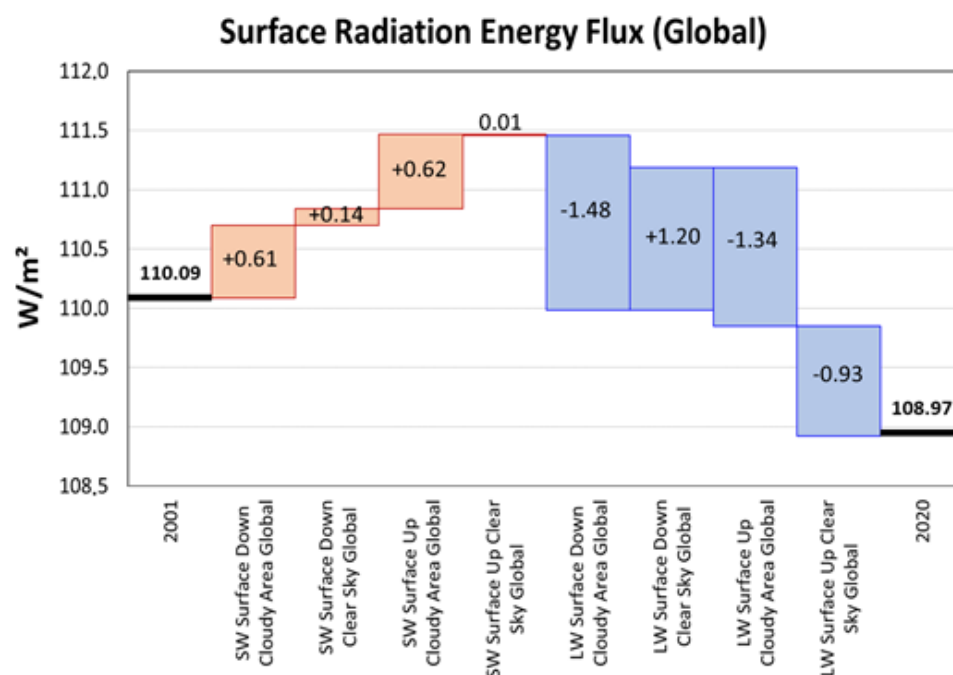
Figure 16. Bridge-chart for the actual changes at the surface from 2001 to 2020 ("start-to-end change").

Please note that the individual effects, shown in Figures 10 and 11, are weighted by the cloud area fraction (ca. 1/3rd for "Clear Sky" and ca. 2/3rd for "Cloudy Areas") and that the sign is positive for increasing downwelling or decreasing upwelling fluxes and vice versa. Reading example: "LW Surface Down Cloudy" in Figure 11c changes from 360.07 to 357.88 W/m^2 = −2.19 W/m^2. Multiplied by 0.674 (67.4% cloud area fraction) gives a contribution of −1.48 W/m^2 from 2001 to 2020.

The rather short period of only 20 years prevents us from answering this key question at this time. Furthermore, there is no validated physical mechanism that led to the declining TOA shortwave emission and to the cloudiness change around the year 2000.

6. Conclusions

Radiative energy flux data from CERES were analyzed and showed in accordance with OHC data a further increasing climate system enthalpy during the period 2001–2020. The total enthalpy rise amounted to about 240 ZJ in these two decades. As Figure 15 shows, the major driving effect was the declining shortwave TOA emission. The TOA outgoing longwave emission has increased and therefore reduced the TOA net flux.

Generating the CERES data is a demanding task and requires sophisticated technology and models which are vulnerable and prone to uncertainties. Liu et al. [28] have pointed out significant uncertainties of satellite datasets and discussed the role of the lateral energy flow. Su et al. [29] have recently pointed out the importance of maintaining the consistency among the components of the measuring system. On the other hand, Loeb et al. [14], Johnson et al. [30] and, also, Dewitte et al. [15] have shown that the CERES net flux agrees well with the independently observed OHC data. This good agreement, also confirmed by our analysis, justifies some confidence in the CERES datasets used.

We could identify the effect of the anthropogenic greenhouse gas emissions from 2001 to 2020 in the "Clear Sky" LW part but not in the "Cloudy Areas" and not in the SW. At the same time, we find, in accordance with the analysis of Loeb et al. [14] and Ollila [18], that the major changes for the TOA energy budget during this period of time stemmed from the clouds for SW and LW, as well as the ground temperature in the LW.

Loeb et al. [14] pointed out, that the direct aerosol effect is rather small, but the indirect effect via the cloud formation may be larger. The shift from a negative to a positive PDO

(Pacific Decadal Oscillation) index as an additional factor for the net TOA flux is mentioned in [14].

Our analysis, which differentiates between clear sky and cloudy areas, support that in view of the historical heating steps shown in Figure 13, that the currently observed high radiative net flux has a large intrinsic component. As shown in Figure 13, the heating phases coincide with the AMO change from negative to positive. It has been shown by several authors that AMO may be an important intrinsic climate factor [31–33]. A similar discussion was held about 20 years ago in papers of Chen et al. [34] and Wielicki et al. [35], both of them emphasized the underestimated decadal natural variabilities in the tropical regions.

The start-to-end bridge charts in Figure 15 (TOA) and Figure 16 (surface) are high-lighting the effect of the "Cloudy Areas" and the shortwave radiation in a slightly different view. In these figures, we look at the actual start and end data, their actual differences from 2001 to 2020, and the actual incremental contribution of each of the radiative categories. Please note, that the increments are weighted by area. In Figure 15 (TOA), the biggest changes originate from the "Cloudy Areas". In Figure 16 (surface) the largest heating impulse stemmed from the increasing downwelling and decreasing upwelling shortwave fluxes in the "Cloudy Areas" (together +1.23 W/m^2), the strongest cooling effect was the decreased longwave downwelling flux in the "Cloudy Areas" (−1.48 W/m^2), followed by increasing LW upwelling fluxes in the "Cloudy Areas" (−1.34 W/m^2) and the "Clear Sky" (−0.93 W/m^2). The change of the longwave downwelling radiation can be interpreted in part as the additional effect of the increased greenhouse gas concentration. For the "Clear Sky" it is +1.20 W/m^2. In the "Cloudy Areas", this effect is negative (−1.48 W/m^2) so that the sum of these values is −0.14 W/m^2. The −0.93 W/m^2 of the "Clear Sky" upwelling longwave should be caused by the increased thermal emission due to the higher surface temperature.

There are distinct differences between the Northern and the Southern hemisphere. Generally speaking, the South was more stable than the North in trends and variances of almost all radiative quantities. This could be due to the larger ocean share of the surface in the South.

Finally, the key issue, i.e., whether the current heating phase is a temporary phase or a permanent phenomenon, can be judged only on the basis of a longer observation time. In the latter case, the physical mechanism behind the "shortwave heating" [18] or a possible "cloud thinning", as discussed by several other authors [36–38] should be understood, because it could accelerate the warming trend. In the former case, the strong net flux of +0.8 W/m^2 should decrease naturally.

has many years of academic experience and a solid publication track record in chemistry and climate science.

Appendix A

Table A1. Statistical Error Analysis of the TOA Fluxes (part1).

Quantity	Intercept	Error of Intercept	Slope	Error of Slope	Trend	Rel. Error
Unit	W/m^2	W/m^2	W/m^2 a	W/m^2 a	W/m^2 dec	%
Inc. Solar Flux in-TOA Global	340.05	0.04	−0.0035	0.0032	−0.03	92
LW Flux out-All Sky-TOA Global	239.99	0.12	0.0284	0.0112	0.28	39
SW Flux out-All Sky-TOA Global	99.64	0.12	−0.0704	0.0107	−0.70	15
Net Flux-All Sky-TOA Global	0.42	0.14	0.0384	0.0130	0.38	34
LW Flux out-Clear Sky-TOA Global	268.14	0.11	0.0044	0.0102	0.04	229
SW Flux out-Clear Sky-TOA Global	53.61	0.07	−0.0372	0.0066	−0.37	18
Net Flux-Clear Sky-TOA Global	18.30	0.09	0.0293	0.0080	0.29	27
LW Flux out-Cloudy Areas-TOA Global	226.45	0.15	0.0346	0.0134	0.35	39
SW Flux out-Cloudy Areas-TOA Global	121.77	0.16	−0.0775	0.0142	−0.78	18
Net Flux-Cloudy Areas-TOA Global	−8.18	0.19	0.0394	0.0167	0.39	42
Inc. Solar Flux in-TOA NH	339.74	0.05	−0.0048	0.0043	−0.05	90
LW Flux out-All Sky-TOA NH	240.53	0.17	0.0344	0.0153	0.34	45
SW Flux out-All Sky-TOA NH	99.66	0.16	−0.0813	0.0145	−0.81	18
Net Flux-All Sky-TOA NH	−0.45	0.17	0.0421	0.0151	0.42	36

Table A1. *Cont.*

Quantity	Intercept	Error of Intercept	Slope	Error of Slope	Trend	Rel. Error
Unit	W/m^2	W/m^2	W/m^2 a	W/m^2 a	W/m^2 dec	%
LW Flux out-Clear Sky-TOA NH	268.87	0.14	0.0174	0.0129	0.17	74
SW Flux out-Clear Sky-TOA NH	56.83	0.10	−0.0616	0.0086	−0.62	14
Net Flux-Clear Sky-TOA NH	14.04	0.09	0.0393	0.0084	0.39	21
LW Flux out-Cloudy Areas-TOA NH	224.88	0.18	0.0469	0.0164	0.47	35
SW Flux out-Cloudy Areas-TOA NH	123.31	0.23	−0.0969	0.0209	−0.97	22
Net Flux-Cloudy Areas-TOA NH	−8.45	0.25	0.0452	0.0221	0.45	49
Inc. Solar Flux in-TOA SH	340.35	0.05	−0.0022	0.0045	−0.02	203
LW Flux out-All Sky-TOA SH	239.45	0.14	0.0224	0.0128	0.22	57
SW Flux out-All Sky-TOA SH	99.61	0.15	−0.0594	0.0134	−0.59	22
Net Flux-All Sky-TOA SH	1.29	0.18	0.0348	0.0158	0.35	45
LW Flux out-Clear Sky-TOA SH	267.41	0.11	−0.0085	0.0100	−0.09	118
SW Flux out-Clear Sky-TOA SH	50.38	0.11	−0.0129	0.0095	−0.13	74
Net Flux-Clear Sky-TOA SH	22.56	0.13	0.0192	0.0118	0.19	61
LW Flux out-Cloudy Areas-TOA SH	227.82	0.17	0.0231	0.0154	0.23	67
SW Flux out-Cloudy Areas-TOA SH	120.09	0.12	−0.0572	0.0111	−0.57	19
Net Flux-Cloudy Areas-TOA SH	−7.56	0.18	0.0319	0.0165	0.32	52

Explanation: "Intercept" is the result of a linear regression, i.e., the estimate for the year 2001. Please note that the first year 2001 was set to zero so that "Intercept" is equal to the linear estimate for the year 2001. "Error Intercept" denotes the statistical standard error. "Slope" is the result of a linear regression. "Error of Slope" denotes the statistical standard error. "Trend" is the slope multiplied by 10 and the "Rel. Error" is the Ratio of "Error of Slope" and "Slope", multiplied by 100.

Table A2. Statistical Error Analysis of the TOA Fluxes (part 2).

Quantity	*p*-Value (Slope)	CI Low (Slope)	CI High (Slope)	Δ CI (Slope)	R^2	Fig.
Unit	1	W/m^2 a	W/m^2 a	W/m^2 a	1	-
Inc. Solar Flux in-TOA Global	0.2937	−0.010	0.003	0.014	0.06	1
LW Flux out-All Sky-TOA Global	0.0204	0.005	0.052	0.047	0.26	2
SW Flux out-All Sky-TOA Global	0.0000	−0.093	−0.048	0.045	0.71	3
Net Flux-All Sky-TOA Global	0.0086	0.011	0.066	0.055	0.33	4
LW Flux out-Clear Sky-TOA Global	0.6674	−0.017	0.026	0.043	0.01	6

Table A2. *Cont.*

Quantity	*p*-Value (Slope)	CI Low (Slope)	CI High (Slope)	Δ CI (Slope)	R^2	Fig.
SW Flux out-Cloudy Areas-TOA SH	0.0001	−0.080	−0.034	0.047	0.60	5
Net Flux-Cloudy Areas-TOA SH	0.0693	−0.003	0.067	0.070	0.17	8

Explanation: The "*p*-value" for the slope is the result of a linear regression. A *p*-value below 0.05 rejects the Null hypothesis (i.e., slope = 0) with 95% confidence. *p*-values below 1E-4 are cut off after four digits. "CI low" is the lower boundary and "CI high" is the upper boundary of the 95% confidence interval for the slope. "Δ CI" is the width of the confidence interval. "R^2" is coefficient of determination and indicates the strength of the correlation. An R^2 near zero means that the respective flux is approximately a constant for the time-period considered. For convenience, "Fig." gives the reference to the figures in this paper.

Table A3. Statistical Error Analysis of the Surface Fluxes (part1).

Quantity	Intercept	Error of Intercept	Slope	Error Slope	Trend	Rel. Error
Unit	W/m^2	W/m^2	W/m^2 a	W/m^2 a	W/m^2 dec	%
SW Flux Down-All Sky-Surface Global	186.35	0.17	0.047	0.015	0.47	32
SW Flux Down-Clear Sky-Surface Global	243.14	0.15	0.000	0.014	0.00	14723
SW Flux Up-All Sky-Surface Global	23.45	0.07	−0.030	0.006	−0.30	22
SW Flux Up-Clear Sky-Surface Global	29.75	0.11	−0.024	0.010	−0.24	41
LW Flux Down-All Sky-Surface Global	344.88	0.37	0.027	0.034	0.27	125
LW Flux Down-Clear Sky-Surface Global	313.18	0.32	0.121	0.029	1.21	24
LW Flux Up-All Sky-Surface Global	397.81	0.25	0.100	0.023	1.00	23
LW Flux Up-Clear Sky-Surface Global	396.84	0.24	0.122	0.022	1.22	18
SW Flux Down-Cloudy Areas-Surface Global	159.04	0.19	0.059	0.017	0.59	29
SW Flux Up-Cloudy Areas-Surface Global	20.42	0.07	−0.034	0.006	−0.34	19
LW Flux Down-Cloudy Areas-Surface Global	360.12	0.46	−0.012	0.041	−0.12	335
LW Flux Up-Cloudy Areas-Surface Global	398.27	0.26	0.090	0.024	0.90	27
SW Flux Net-All Sky-Surface Global	162.90	0.16	0.077	0.015	0.77	19
SW Flux Net-Clear Sky-Surface Global	213.39	0.11	0.024	0.010	0.24	42
SW Flux Net-Cloudy Areas-Surface Global	138.61	0.20	0.093	0.018	0.93	19
LW Flux Net-All Sky-Surface Global	−52.93	0.26	−0.073	0.023	−0.73	32
LW Flux Net-Clear Sky-Surface Global	−83.66	0.13	−0.001	0.012	−0.01	1188
LW Flux Net-Cloudy Areas-Surface Global	−38.15	0.37	−0.102	0.033	−1.02	33
LW + SW-All Sky-Surface Global	109.96	0.25	0.004	0.022	0.04	579
LW + SW-Clear Sky-Surface Global	129.73	0.16	0.023	0.015	0.23	65
LW + SW-Cloudy Areas-Surface Global	100.46	0.37	−0.009	0.034	−0.09	364

Explanation: "Intercept" is the result of a linear regression, i.e., the estimate for the year 2001. Please note that the first year 2001 was set to zero so that "Intercept" is equal to the linear estimate for the year 2001. "Error Intercept" denotes the statistical standard error. "Slope" is the result of a linear regression. "Error of Slope" denotes the statistical standard error. "Trend" is the slope multiplied by 10 and the "Rel. Error" is the Ratio of "Error of Slope" and "Slope", multiplied by 100.

Table A4. Statistical Error Analysis of the Surface Fluxes (part2).

Quantity	*p*-Value (SLOPE)	CI Low (slope)	CI High (Slope)	Δ CI (Slope)	R^2	Fig.
Unit	1	W/m^2 a	W/m^2 a	W/m^2 a	1	-
SW Flux Down-All Sky-Surface Global	0.0064	0.015	0.079	0.064	0.35	10
SW Flux Down-Clear Sky-Surface Global	0.9947	−0.029	0.029	0.057	0.00	10
SW Flux Up-All Sky-Surface Global	0.0002	−0.044	−0.016	0.027	0.54	10
SW Flux Up-Clear Sky-Surface Global	0.0246	−0.044	−0.003	0.041	0.25	10
LW Flux Down-All Sky-Surface Global	0.4327	−0.044	0.098	0.142	0.03	11
LW Flux Down-Clear Sky-Surface Global	0.0006	0.059	0.182	0.123	0.49	11
LW Flux Up-All Sky-Surface Global	0.0004	0.052	0.148	0.096	0.52	11
LW Flux Up-Clear Sky-Surface Global	0.0000	0.076	0.167	0.091	0.64	11
SW Flux Down-Cloudy Areas-Surface Global	0.0032	0.022	0.095	0.073	0.39	10
SW Flux Up-Cloudy Areas-Surface Global	0.0000	−0.048	−0.021	0.027	0.61	10
LW Flux Down-Cloudy Areas-Surface Global	0.7685	−0.099	0.074	0.173	0.00	11
LW Flux Up-Cloudy Areas-Surface Global	0.0014	0.040	0.140	0.100	0.44	11

Table A4. *Cont.*

Quantity	*p*-Value (SLOPE)	CI Low (slope)	CI High (Slope)	Δ CI (Slope)	R²	Fig.
SW Flux Net-All Sky-Surface Global	0.0001	0.046	0.107	0.061	0.61	10
SW Flux Net-Clear Sky-Surface Global	0.0290	0.003	0.045	0.042	0.24	10
SW Flux Net-Cloudy Areas-Surface Global	0.0001	0.055	0.131	0.076	0.60	10
LW Flux Net-All Sky-Surface Global	0.0059	−0.122	−0.024	0.098	0.35	11
LW Flux Net-Clear Sky-Surface Global	0.9339	−0.026	0.024	0.049	0.00	11
LW Flux Net-Cloudy Areas-Surface Global	0.0067	−0.172	−0.032	0.140	0.34	11
LW + SW -All Sky-Surface Global	0.8647	−0.043	0.051	0.094	0.00	12
LW + SW -Clear Sky-Surface Global	0.1405	−0.008	0.054	0.062	0.12	-
LW + SW -Cloudy Areas-Surface Global	0.7865	−0.080	0.061	0.141	0.00	-

Explanation: The "*p*-value" for the slope is the result of a linear regression. A *p*-value below 0.05 rejects the Null hypothesis (i.e., slope = 0) with 95% confidence. *p*-values below 1E-4 are cut off after four digits. "CI low" is the lower boundary and "CI high" is the upper boundary of the 95% confidence interval for the slope. "Δ CI" is the width of the confidence interval. "R²" is coefficient of determination and indicates the strength of the correlation. An R^2 near zero means that the respective flux is approximately a constant for the time period considered. For convenience, "Fig." gives the reference to the figures in this paper.

References

1. Hansen, J.; Nazarenko, L.; Ruedy, R.; Sato, M.; Willis, J.; Del Genio, A.; Koch, D.; Lacis, A.; Lo, K.; Menon, S.; et al. Earth's energy imbalance: Confirmation and implications. *Science* **2005**, *308*, 1431–1435. [CrossRef] [PubMed]

2. Hansen, J.; Sato, M.; Kharecha, P.; von Schuckmann, K. Earth's energy imbalance and implications. *Atmos. Chem. Phys.* **2011**, *11*, 13421–13449. [CrossRef]

3. Trenberth, K.E.; Fasullo, J.T.; Balmaseda, M.A. Earth's Energy Imbalance. *J. Clim.* **2014**, *27*, 3129–3144. [CrossRef]

4. Dewitte, S.; Clerbaux, N. Measurement of the Earth Radiation Budget at the Top of the Atmosphere—A Review. *Remote Sens.* **2017**, *9*, 1143. [CrossRef]

5. Kato, S.; Rose, F.G.; Rutan, D.A.; Thorsen, T.; Loeb, N.G.; Doelling, D.R.; Huang, X.; Smith, W.L.; Su, W.; Ham, S.-H. Surface Irradiances of Edition 4.0 Clouds and the Earth's Radiant Energy System (CERES) Energy Balanced and Filled (EBAF) Data Product. *J. Clim.* **2018**, *31*, 4501–4527. [CrossRef]

6. Loeb, N.G.; Doelling, D.R.; Wang, H.; Su, W.; Nguyen, C.; Corbett, J.G.; Liang, L.; Mitrescu, C.; Rose, F.G.; Kato, S. Clouds and the Earth's Radiant Energy System (CERES) Energy Balanced and Filled (EBAF) Top-of-Atmosphere (TOA) Edition-4.0 Data Product. *J. Clim.* **2018**, *31*, 895–918. [CrossRef]

7. Levitus, S.; Antonov, J.I.; Boyer, T.P.; Baranova, O.K.; Garcia, H.E.; Locarnini, R.A.; Mishonov, A.V.; Reagan, J.R.; Seidov, D.; Yarosh, E.S.; et al. World ocean heat content and thermosteric sea level change (0–2000 m), 1955–2010. *Geophys. Res. Lett.* **2012**, *39*. [CrossRef]

8. Abraham, J.P.; Baringer, M.; Bindoff, N.; Boyer, T.; Cheng, L.; Church, J.A.; Conroy, J.L.; Domingues, C.M.; Fasullo, J.; Gilson, J.; et al. A review of global ocean temperature observations: Implications for ocean heat content estimates and climate change. *Rev. Geophys.* **2013**, *51*, 450–483. [CrossRef]

9. Cheng, L.; Trenberth, K.E.; Fasullo, J.; Boyer, T.; Abraham, J.; Zhu, J. Improved estimates of ocean heat content from 1960 to 2015. *Sci. Adv.* **2017**, *3*, e1601545. [CrossRef]

10. Cheng, L.; Zhu, J.; Abraham, J.; Trenberth, K.E.; Fasullo, J.T.; Zhang, B.; Yu, F.; Wan, L.; Chen, X.; Song, X. 2018 Continues Record Global Ocean Warming. *Adv. Atmos. Sci.* **2019**, *36*, 249–252. [CrossRef]

11. Gebbie, G.; Huybers, P. The Little Ice Age and 20th-century deep Pacific cooling. *Science* **2019**, *363*, 70–74. [CrossRef]

12. Meyssignac, B.; Boyer, T.; Zhao, Z.; Hakuba, M.Z.; Landerer, F.W.; Stammer, D.; Köhl, A.; Kato, S.; L'Ecuyer, T.; Ablain, M.; et al. Meas-uring Global Ocean Heat Content to Estimate the Earth Energy Imbalance. *Front. Mar. Sci.* **2019**, *6*, 432. [CrossRef]

13. Von Schuckmann, K.; Cheng, L.; Palmer, M.D.; Hansen, J.; Tassone, C.; Aich, V.; Adusumilli, S.; Beltrami, H.; Boyer, T.; Cuesta-Valero, F.J.; et al. Heat stored in the Earth system: Where does the energy go? *Earth Syst. Sci. Data* **2020**, *12*, 2013–2041. [CrossRef]

14. Loeb, N.G.; Johnson, G.C.; Thorsen, T.J.; Lyman, J.M.; Rose, F.G.; Kato, S. Satellite and Ocean Data Reveal Marked In-crease in Earth's Heating Rate. *Geophys. Res. Lett.* **2021**, *48*, e2021GL093047. [CrossRef]

15. Dewitte, S.; Clerbaux, N.; Cornelis, J. Decadal Changes of the Reflected Solar Radiation and the Earth Energy Imbalance. *Remote Sens.* **2019**, *11*, 663. [CrossRef]

16. Loeb, N.; Thorsen, T.; Norris, J.; Wang, H.; Su, W. Changes in Earth's Energy Budget during and after the "Pause" in Global Warming: An Observational Perspective. *Climate* **2018**, *6*, 62. [CrossRef]

17. Wong, T.; Stackhouse Jr, P.W.; Kratz, D.P.; Sawaengphokhai, P.; Wilber, A.C.; Gupta, S.K.; Loeb, N.G. State of the Climate in 2019. *Bull. Am. Meteorol. Soc.* **2020**, *101*, S66–S69.

18. Ollila, A. The Pause End and Major Temperature Impacts during Super El Niños are Due to Shortwave Radiation Anomalies. *Phys. Sci. Int. J.* **2020**, 1–20. [CrossRef]

19. Stephens, G.L. Cloud Feedbacks in the Climate System: A Critical Review. *J. Clim.* **2005**, *18*, 237–273. [CrossRef]
20. Karlsson, K.-G.; Anttila, K.; Trentmann, J.; Stengel, M.; Solodovnik, I.; Meirink, J.F.; Devasthale, A.; Kothe, S.; Jääskeläinen, E.; Sedlar, J.; et al. *CLARA-A2.1: CM SAF CLoud, Albedo and Surface RAdiation Dataset from AVHRR Data—Edition 2.1*; EUMETSAT: Darmstadt, Germany, 2020. [CrossRef]
21. Hartmann, D.L.; Ceppi, P. Trends in the CERES Dataset, 2000–2013: The Effects of Sea Ice and Jet Shifts and Comparison to Climate Models. *J. Clim.* **2014**, *27*, 2444–2456. [CrossRef]
22. Svensmark, H. *FORCEMAJEURE—The Sun's Role in Climate Change*; The Global Warming Policy Foundation: London, UK, 2019; ISBN 978-0-9931190-9-5.
23. Shaviv, N.J. On climate response to changes in the cosmic ray flux and radiative budget. *J. Geophys. Res. Space Phys.* **2005**, *110*. [CrossRef]
24. Roemmich, D.; A Church, J.; Gilson, J.; Monselesan, D.; Sutton, P.; Wijffels, S. Unabated planetary warming and its ocean structure since 2006. *Nat. Clim. Chang.* **2015**, *5*, 240–245. [CrossRef]
25. Baggenstos, D.; Häberli, M.; Schmitt, J.; Shackleton, S.A.; Birner, B.; Severinghaus, J.P.; Kellerhals, T.; Fischer, H. Earth's radiative imbalance from the Last Glacial Maximum to the present. *Proc. Natl. Acad. Sci. USA* **2019**, *116*, 14881–14886. [CrossRef] [PubMed]
26. Allan, R.P.; Liu, C.; Loeb, N.G.; Palmer, M.D.; Roberts, M.; Smith, D.; Vidale, P.-L. Changes in global net radiative imbalance 1985–2012. *Geophys. Res. Lett.* **2014**, *41*, 5588–5597. [CrossRef]
27. Wild, M. Global dimming and brightening: A review. *J. Geophys. Res. Space Phys.* **2009**, *114*, 114. [CrossRef]
28. Liu, C.; Allan, R.P.; Mayer, M.; Hyder, P.; Loeb, N.G.; Roberts, C.; Valdivieso, M.; Edwards, J.M.; Vidale, P.-L. Evaluation of satellite and reanalysis-based global net surface energy flux and uncertainty estimates. *J. Geophys. Res. Atmos.* **2017**, *122*, 6250–6272. [CrossRef]
29. Su, W.; Liang, L.; Wang, H.; Eitzen, Z.A. Uncertainties in CERES Top-of-Atmosphere Fluxes Caused by Chang-es in Accompanying Imager. *Remote Sens.* **2020**, *12*, 2040. [CrossRef]
30. Johnson, G.C.; Lyman, J.M.; Loeb, N.G. Improving estimates of Earth's energy imbalance. *Nat. Clim. Chang.* **2016**, *6*, 639–640. [CrossRef]
31. Chylek, P.; Klett, J.D.; Lesins, G.; Dubey, M.K.; Hengartner, N. The Atlantic Multidecadal Oscillation as a dominant factor of oceanic influence on climate. *Geophys. Res. Lett.* **2014**, *41*, 1689–1697. [CrossRef]
32. Kravtsov, S.; Grimm, C.; Gu, S. Global-scale multidecadal variability missing in state-of-the-art climate models. *Npj Clim. Atmos. Sci.* **2018**, *1*, 34. [CrossRef]
33. Zhou, J.; Tung, K.-K. Deducing Multidecadal Anthropogenic Global Warming Trends Using Multiple Regression Analysis. *J. Atmos. Sci.* **2013**, *70*, 3–8. [CrossRef]
34. Chen, J.; Carlson, B.E.; Del Genio, A.D. Evidence for Strengthening of the Tropical General Circulation in the 1990s. *Science* **2002**, *295*, 838–841. [CrossRef] [PubMed]
35. Wielicki, B.A.; Wong, T.; Allan, R.P.; Slingo, A.; Kiehl, J.T.; Soden, B.J.; Gordon, C.T.; Miller, A.J.; Yang, S.-K.; Randall, D.A.; et al. Evidence for large decadal variability in the tropical mean radiative en-ergy budget. *Science* **2002**, *295*, 841–844. [CrossRef] [PubMed]
36. Kubar, T.L.; Jiang, J.H. Net Cloud Thinning, Low-Level Cloud Diminishment, and Hadley Circulation Weak-ening of Precipitating Clouds with Tropical West Pacific SST Using MISR and Other Satellite and Reanalysis Data. *Remote Sens.* **2019**, *11*, 1250. [CrossRef]
37. Del Genio, A.D.; Wolf, A.B. The Temperature Dependence of the Liquid Water Path of Low Clouds in the Southern Great Plains. *J. Clim.* **2000**, *13*, 3465–3486. [CrossRef]
38. Gordon, N.D.; Klein, S.A. Low-cloud optical depth feedback in climate models. *J. Geophys. Res. Atmos.* **2014**, *119*, 6052–6065. [CrossRef]